ADVANCED MATERIALS INTERFACES
Open Access
www.advmatinterfaces.de

Controlled Stratification and Assembly of Cellulose Nanocrystals in Polymeric Films Toward Optically Active Coatings

*Farid Khelifa, Heike M. A. Ehmann, Abderrahman Lamaoui, Mathieu Surin, Jenifer Rubio-Magnieto, Philippe Dubois, and Youssef Habibi**

Nature's most brilliant hues arise from the interaction of light with multilayered- structures of aligned building blocks. Mimicking this hierarchical organization in highly-ordered thin films of liquid crystalline species has attracted increasing attention for potential applications in sensors and optical switching displays. Due to its intriguing ability to organize into optically active materials, cellulose nanocrystals (CNCs) are attracting a strong interest in the scientific community. This study demonstrates that the shear-driven convective assembly technique can be used to stratify in a controlled fashion highly ordered multilayers of rod-like CNC embedded in a protective hydrophobic polymer matrix leading to optically active thin films. The films remain fully transparent even after stratifying 50 layers. Atomic force microscopy analysis reveals that over 87% of the CNCs in the upper layer aligned within ±20° of the withdrawal direction. Notably, the stratification does not disrupt the organization of the underlying layers. The films exhibit strong selective reflections with uniform and intense colors, dependent on the number of stratified layers. This scalable appraoch enables precise control over the optical characteristics of CNC-polymer composite films, presenting opportunities for environmentally friendly applications in pigment-free coatings, security papers, and optical devices.

1. Introduction

Nature constitutes a wonderful source of inspiration for the design of new structured materials by mimicking the hierarchical organization of natural species and replicating their functionalities such as colors, mechanical performances, water repulsion, etc.[1] Regarding coloration, many natural biological systems develop wonderful sets of colors originating from pigments, bioluminescence, or structural colors.[2,3] The later coloration, often referred to as structural coloration, is commonly observed in many animals and insects such as butterflies, feathers of birds, and crustacean shells and has diverse arrays of functions like mate attraction, camouflage, water repulsion, UV protection, etc. Hence, structural coloration in biological systems is obtained without using pigments, or luminescence but originates from multilayer-based photonic structures that selectively reflect visible light due to a periodic modulation of the refractive index. These multilayered structures are built often from stacked layers of chitin (in animal) or cellulose (in plant) fibrils embedded in other cell components.

The recent advances in modern engineering and technology have hastened the development of bioinspired nanostructured thin films with tailored optical properties.[4] Cellulose Nanocrystals (CNCs), derived from cellulose fibers by controlled

F. Khelifa, P. Dubois
Laboratory of Polymeric and Composite Materials
Center of Innovation and Research in Materials & Polymers (CIRMAP)
Institute of Research in Science and Engineering of Materials
University of Mons – UMONS
Place du Parc, Mons 23-7000, Belgium

The ORCID identification number(s) for the author(s) of this article can be found under https://doi.org/10.1002/admi.202400608

DOI: 10.1002/admi.202400608

H. M. A. Ehmann
Institute for Chemistry and Technology of Materials
NAWI Graz
Graz University of Technology
Stremayrgasse 9, Graz 8010, Austria

H. M. A. Ehmann
Anton-Paar GmbH
Anton-Paar-Straße 20, Graz 8054, Austria

A. Lamaoui, Y. Habibi
Sustainable Materials Research Center (SUSMAT – RC)
Mohammed VI Polytechnic University (UM6P)
Lot 660, Hay Moulay Rachid Ben Guerir 43150, Morocco
E-mail: Youssef.habibi@um6p.ma

M. Surin, J. Rubio-Magnieto
Laboratory for Chemistry of Novel Materials
Center of Innovation and Research in Materials & Polymers (CIRMAP)
University of Mons – UMONS
23 Place du Parc, Mons B-7000, Belgium

acid-catalyzed hydrolysis, have attracted particular attention due to their impressive optical properties among others.[5,6] Colloidal aqueous suspensions of CNC are well-known to spontaneously organize and, upon reaching a certain concentration, to exhibit nematic or chiral nematic liquid crystal ordering similar to other rigid rod-like species, such as tobacco mosaic virus,[7] poly(tetrafluoroethylene),[8] boehmite,[9] filamentous phage,[10] and DNA fragments.[11] This cholesteric structure observed in suspension is often described as a helical assembly (around a cholesteric axis) of planes of rod-like crystals that are arranged in a stacked configuration, aligning along a direction. The angle of the director exhibits incremental changes in each successive plane.[5] Moreover, this structured arrangement can be maintained through a controlled drying process of the suspensions. This preservation results in iridescent films of CNC exhibiting a chiral nematic pitch on the same length scale as the wavelength of visible light. These solid films have a huge range of potential applications such as photonic encryption,[12] sensors,[13] actuators,[14] anticounterfeiting smart tags[15] or to produce light shutters.[16] They serve also as templates to create mesoporous cellulose,[17] silica,[18] and carbon[19] materials with tunable chiral nematic structures.

More intriguing is that the iridescence of CNC films can be easily adapted by tuning the chiral nematic pitch either by adjusting the ionic strength of the medium through the addition of electrolytes,[20] or by varying the pH,[21] the evaporation rate,[22] thickness[23] or the nature of the substrate.[24]

However, it is important to highlight that these films lack freestanding characteristics due to the inherent high fragility of CNC.[25] Moreover, from the viewpoint of practical applicability, films made of pure CNC obtained from aqueous suspensions are unsuitable due to their hygroscopic nature, which is associated with the intrinsic hydrophilic properties of cellulose. To overcome this, several strategies have been recently attempted to access optically active films through the incorporation of CNC in polymer matrices, mainly by solvent casting technique.[26–28] However, this approach faces challenges in maintaining uniformity and control of the photonic structure within the polymer matrix since preserving the optical activity is strongly affected by many parameters like the viscosity of the surrounding environment. A notable approach involves Langmuir–Blodgett (LB) film deposition, which offers precise control over the packing density and orientation of anisotropic nanoparticles at a monolayer level. In a recent study, four layers of rod-shaped CNCs were uniaxially deposited using LB techniques, enabling accurate characterization of their anisotropic material properties.[29] However, LB deposition faces limitations in scalability and involves complex experimental setups.

Our previous work addressed some of these challenges by demonstrating the feasibility of convective-assisted assembly, a rapid, scalable, and cost-effective deposition method, to produce highly organized and stable monolayer films of poly(2-ethylhexyl acrylate-co-glycidyl methacrylate) (poly(EHA-co-GMA)) with a high loading of CNCs.[30] These monolayer films were characterized by poor hygroscopicity that limits their degradation in humid atmospheres.[31] Herein we extend our approach to stratify multilayers of these highly ordered CNC films using a convective-driven method resulting in the creation of a birefringent material. The layer-by-layer methodology to fabricate iridescent optical coatings of CNCs in aqueous medium on silicon wafers has been reported by Zhao via spin-coating.[32] However, this process may lead to challenges such as non-uniform coating thickness, limited scalability, and potential disruptions in the long-range order of CNCs. Through in-depth optimization of stratified layers, we show for the first time that such stratification reveals that the resulting multilayers yield optically active CNC-based films in an acrylic matrix with tunable coloration based on their thickness. Thin films made of stacked layers show unique morphological and optical properties, as characterized by Atomic Force Microscopy (AFM), Linear Dichroism (LD), Circular Dichroism (CD), UV–vis absorption spectroscopies, and polarized optical microscopy. Since the cross-section of CNCs is in the range of small-angle X-ray scattering (SAXS)[20,33] the alignment was further studied using synchrotron radiation in gracing incidence configuration.

2. Results

CNC suspensions were combined with poly(EHA-co-GMA) to obtain a solution of CNCs/poly(EHA-co-GMA) with a weight ratio of 50/50. The deposition of the solution on glass substrates was carried out using a shear-convective assembly to form multilayered films, as detailed in the Experimental Section. The deposited films remained fully transparent even after the stratification of 50 layers (**Figure 1a**). However, it is important to note that the transparency observed is qualitative, based on visual inspection rather than quantitative measurements such as % transmittance. The nanocomposite films exhibited high compactness with a measured thickness of ≈20 µm as depicted in scanning electron microscopy (SEM) micrographs (Figure 1b). This corresponds to an individual layer thickness of ≈0.4 µm. The alignment of CNCs stratification in a uniform direction was also evaluated through SEM micrographs (Figure 1c).

Morphological analyses of the upper layer, conducted through Peak Force Tapping AFM, unveiled flat, homogeneous, and densely packed CNCs-based thin coatings. Notably, particles tended to align in the withdrawal direction (**Figure 2**). The cause of this unidirectional deposition is elucidated through shear-driven alignment, a phenomenon observed when rod-like nanoparticles undergo shearing forces. The origin of this phenomenon is associated with a delicate equilibrium of various mutual forces and interactions, notably hydrodynamic forces (shear and drag), Brownian motion (viscosity), surface tension (capillary forces), and electrostatic interactions.[30,34]

AFM images (Figure 2a,c,e,g) show that CNCs in the upper layer are highly oriented toward the withdrawal direction of deposition. To assess the alignment degree of CNCs within the top layer, Gwyddion software was employed for analysis, as detailed in a previous study.[35] Each CNC was individually assigned a director vector, and the relative angle of each vector concerning the withdrawal direction was subsequently calculated and the results are presented in Figure 2b,d,f,h. The films were then categorized into different groups depending on the number of CNCs falling into the following angle ranges 0–20°; 20–40°; 40–60° and 60–90°. Taking into account the symmetry conditions for angles spanning from -90° to 0°, counts were combined with their respective positive angles. Regardless to the layer count, over 87% of the CNCs exhibit alignment within a range of ±20°

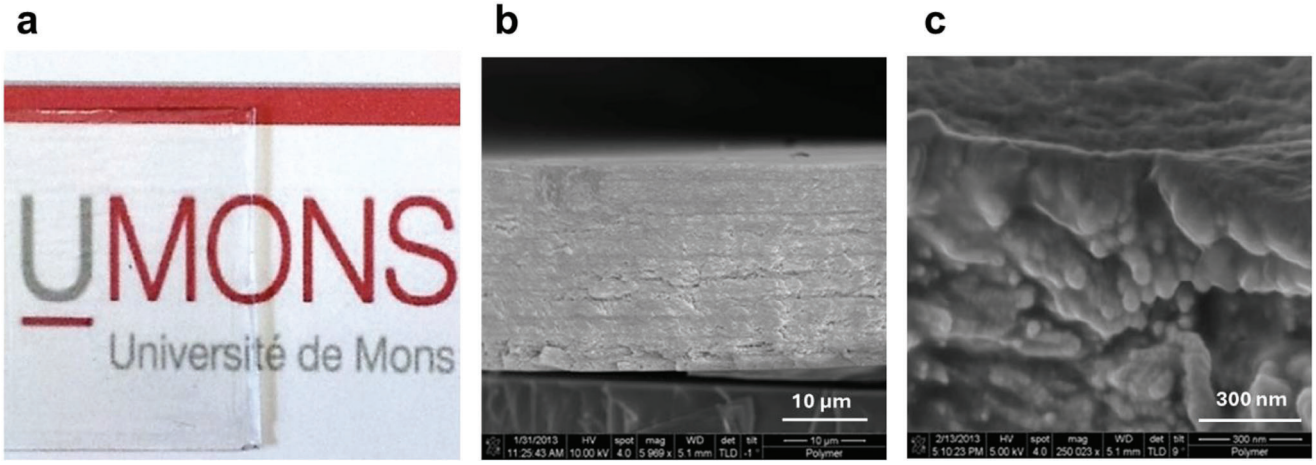

Figure 1. a) Picture illustrating transparency of CNCs/poly(EHA-co-GMA) thin film comprising 50 layers deposited on a glass substrate using the shear-convective method, and b,c) the corresponding feature SEM images depicting the cross-section of the thin film.

relative to the withdrawal direction (Table S1, Supporting Information). The remarkable degree of alignment observed is primarily attributed to the prevailing shear forces, as electrostatic interactions between CNC-CNC and CNC-substrate are diminished or potentially excluded in favor of robust CNCs-poly(EHA-co-GMA) interactions, as previously demonstrated in the casting process.[36] While the alignment achieved in this investigation is similar to that attained for aqueous suspensions of CNCs with the utilization of the identical deposition method, the presence of the polymer seems to foster further organization. Notably, the degree of alignment of CNCs in the poly(EHA-co-GMA), generated through this cost-effective, straightforward, and swift technique, exceeds that achieved with more complex methods, such as those involving strong magnetic fields.[37,38] It is worth mentioning that the accumulation of layers does not impact the alignment of the upper layer, with over 87% of CNC still oriented within ± 20° relative to the withdrawal direction (Table S1, Supporting Information). Furthermore, the deposition of the upper layer does not alter the organization of the sublayers as confirmed by Grazing-Incidence Small-Angle X-ray Scattering (GISAXS) and by LD experiments.

In **Figure 3** the *q*-plots of the GISAXS experiments are shown (3.1–3.3), whereby the samples were either aligned parallel (a-series) or perpendicular (b-series) to the beam. Further, the c-series are the 1D cuts in the q_y direction, while the d-series represent the 1D cut in the q_z direction of both alignments. In Figure 3(1.a,b), it can be seen that if solely the copolymer (relatively thick layer, as it was impossible to control the deposition of continuous monolayer layer) is deposited, a highly ordered pattern in both alignments (parallel and perpendicular, respectively) is visible in the corresponding *q*-plot. The scattering in q_z and q_y directions appears very narrow, indicating that only a few scattering centers are accessible within the GISAXS size range and that the structural features exceed the size of 50 nm for both alignments. Nevertheless, a distinct shape is visible when probing the samples either parallel or perpendicular to the deposition direction. In the case of probing parallel to the deposition direction, slight rings are visible at $q_y = 1.311\ nm^{-1}$ (d = 4.8 nm) and $1.715\ nm^{-1}$ (d = 3.7 nm) (i.e., the rings visible within the q_z range, measured at their out of plane presence). Those indicate the presence of a higher order of the copolymer itself in a repeating manner. Contrarily, perpendicular to the beam (Figure 3(1.b)), the scattering pattern is very narrow and the rings of Figure 3(1.a) are less pronounced but still visible in their respective 1D cuts. The peak in the q_y plane corresponds to the d = 3.7 nm while the one at 4.8 nm is absent. This can be explained by the alignment of the polymer with respect to the incidence beam. In general, the behavior of the rings, e.g., pronounced smearing when probed parallel to the beam and narrowing when probed perpendicular to the beam; proves the presence of lamellar structures of the copolymer in use (see Figure 3). It is known that disordered films or partially ordered or even thick films with many layers result in rings being dominant, originating from q_z and ending in the Yoneda regime (q_y cut). For structures aligned parallel to the surface regular spaced stripes of intensity along the q_z direction are noted (i.e., Bragg sheets). If structures are aligned perpendicular with respect to the surface (e.g., chain stretching from polymers toward the interface), rod-like correlation peaks appear, similar to those observed in grazing incidence diffraction. This indicates that the q_z rings of the copolymer (slightly diffused Bragg sheets) can be correlated to spacing that occurs parallel to the surface, i.e., the layer deposition/thickness. These observations were furthermore more correlated by 2D-FFT of the AFM images of the films.

In Figure 3(2.a,b) the copolymer-CNCs deposition of one layer is shown. Compared to the pattern of the copolymer alone (Figure 3(1)), we observe that the introduction of aligned CNC leads to an introduction of polydispersive scattering centers (broadening of scattering intensity next to the reflected beam behind the beam stop). Nevertheless, even if CNCs with their varying lengths and widths are introduced within this aligned composite film, the alignment is still clearly visible even if the perfection of solely using the polymer is slightly distorted. The shoulder is still visible ≈3.6 nm in the q_z-cut (measured in the out-of-plane regime). The 1D cut in the q_y direction (Figure 3(1.c)) reveals that the slope is less pronounced, showing the contribution of the new scattering centers of the CNC rods with their varying widths and lengths, as well as pore structures, broaden and

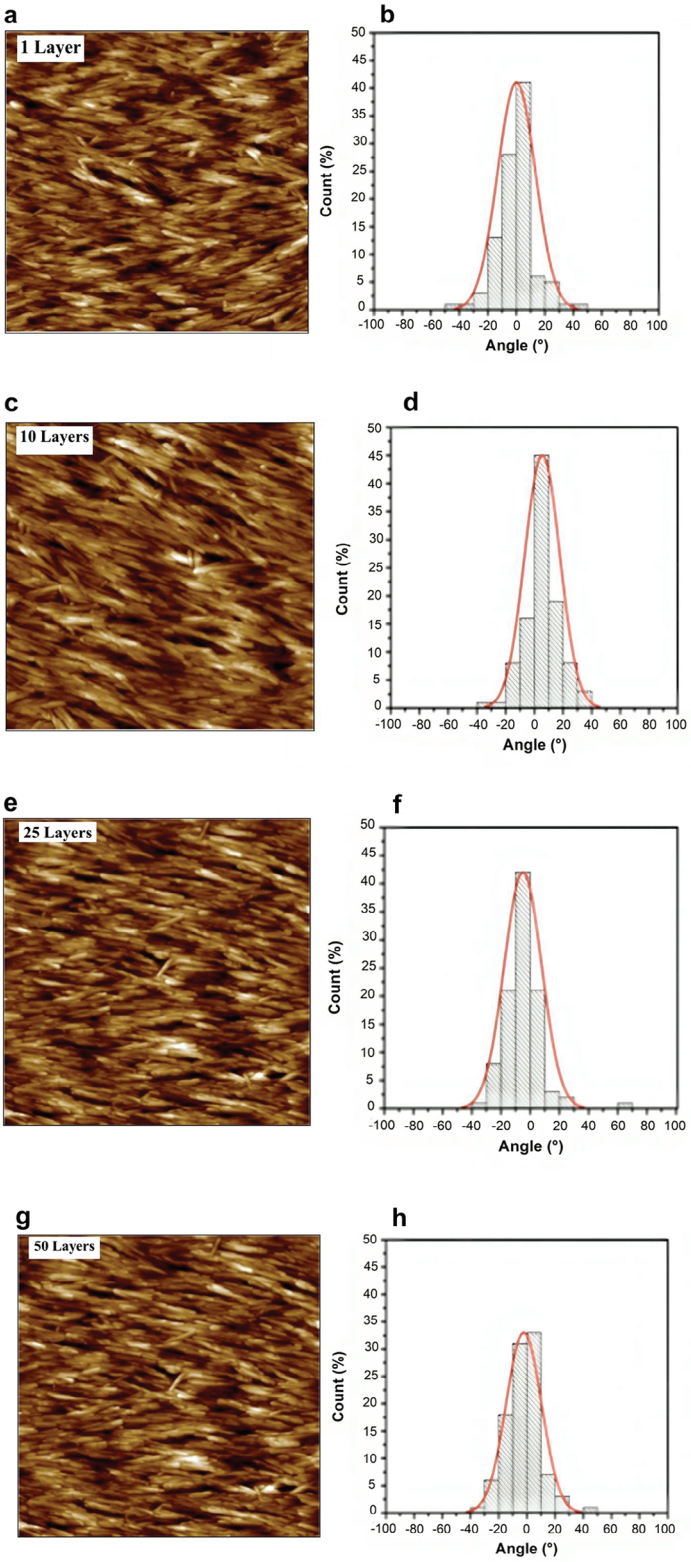

Figure 2. Peak Force Tapping-mode height images (2.0 × 2.0 μm^2) of CNCs/poly(EHA-co-GMA) thin films with 1 layer (a), 10 layers (c), 25 layers (e) and 50 layers (g) alongside the corresponding alignment distribution of the upper layer with respect to the withdrawal direction (b, d, f and h).

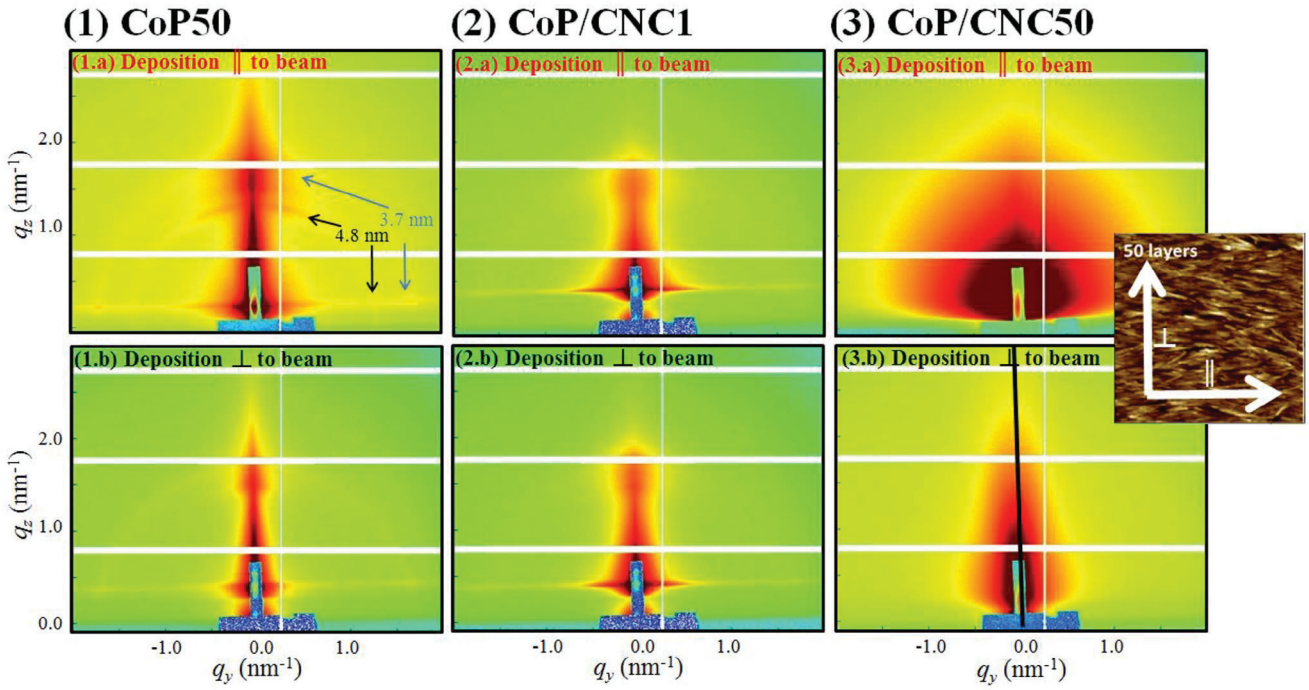

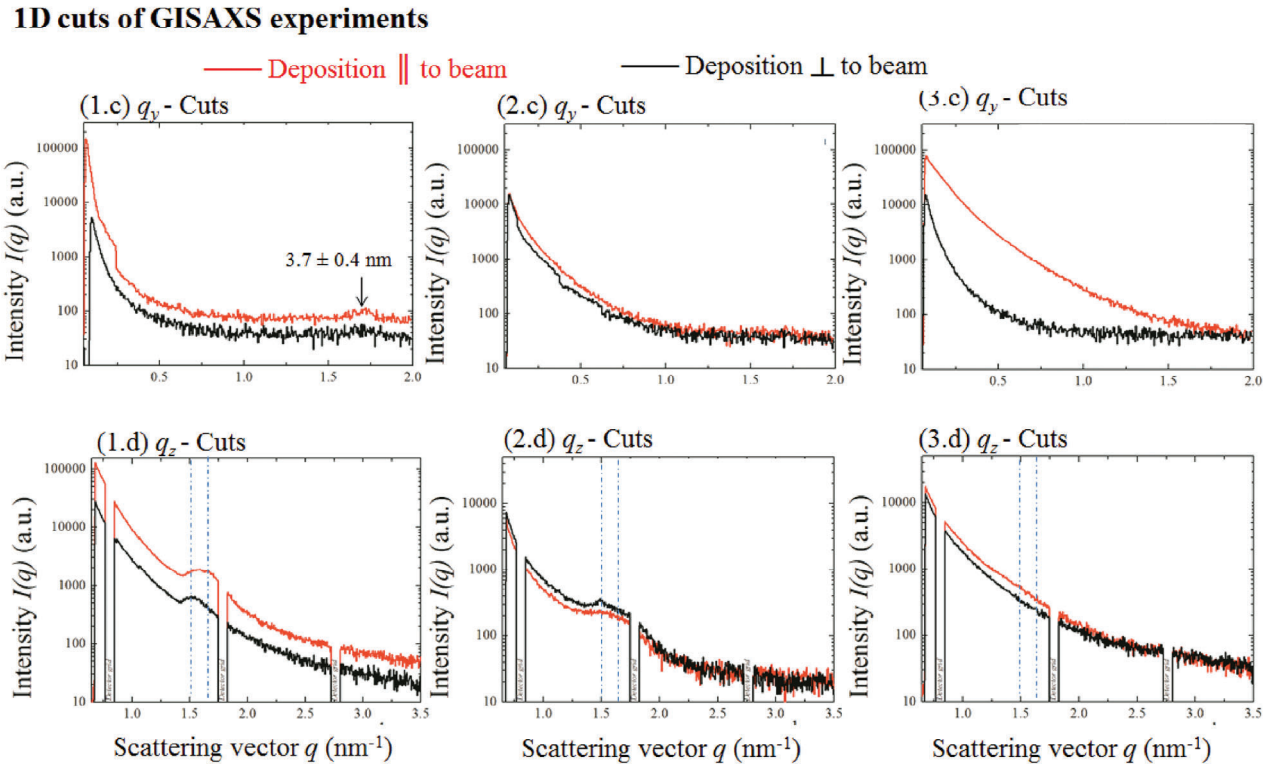

Figure 3. q-plots of 1) one layer of the copolymer, 2) one layer of the copolymer with CNC and 3) 50 layers of the copolymer with CNCs (upper row a) measured with deposition direction being parallel to beam; lower row b) measured with deposition direction being perpendicular to the beam) and their corresponding 1D cuts with c) along the q_y and d) along the q_z direction.

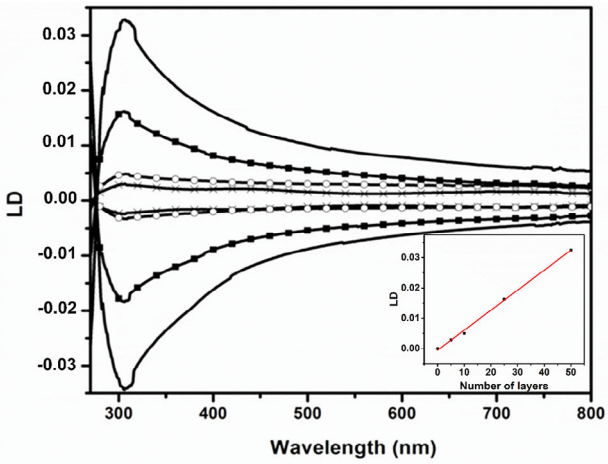

Figure 4. Linear dichroism spectra of CNCs/poly(EHA-co-GMA) materials consisting of 5 layers (X), "10 layers" (**O**), "25 layers" (■) and "50 layers" (line) when they are aligned parallel (positive signal) and perpendicular (negative signal) to the incident cross-polarized light. Inset: the maximum intensity reported as a function of the number of layers.

distort the appearance of the pattern. This effect is even more dramatic when 50 layers are deposited as shown in Figure 3(3) where especially the deposition parallel to the beam (**3**.3a) shows a broad halo around the reflected beam stop. Since this distinct broadening is absent when the sample is rotated (**3**.3b, perpendicular to the beam), it can be followed that the direction-dependent broadening originates from the alignment of the CNCs within the copolymer matrix. Especially the q_y-cut (**3**.3c) reveals that parallel to the beam more scattering centers in the region of the GISAXS experiment contribute to the overall scattering (e.g., interplay of distances between the CNCs as well as their width). Since the beam configuration was slit-like, the cross-section of many CNCs is illuminated, which contributes to this halo (d_{range} ≈4 – 80 nm). Furthermore, it can be seen that the synchrotron X-ray beam penetrates the underlying layers that leads in the perpendicular probed sample to a more pronounced broadening as if only 1 CNC layer is deposited, but this is of minor weighting since the orientation of the upper layer is still dominating and clearly visible when the sample is rotated. The peaks, still present in the 1-layer deposition of the copolymers vanish in the *q*-pattern of the 50-layer deposition (Figure 3(3.d)). This can be explained by the fact that since they were only slightly present, the scattering contribution of the underlying layers smears them "away" and only a slight shoulder is visible within the q_z-plot with a (blue line indicated in d series; q_y-d value of 3.7 nm). When 10 layers are deposited (data not shown) those peaks originating from the copolymer are still clearly visible in the perpendicular cut, but this is no longer dominant when 25 layers are applied.

Furthermore, in order to evaluate the influence of the deposition on the alignment of sublayers, LD spectroscopy measurements were also performed on films containing from 5 layers up to 50 layers (**Figure 4**). LD spectroscopy can provide valuable information about the alignment of particles.[39,40] With the help of LD spectroscopy, the study explores the variation in absorption between parallel and perpendicular linearly polarized light concerning the orientation axis of particles.[41]

In the case of CNCs/poly(EHA-co-GMA) monolayer, the intensity was insufficient to register the LD signal. However, beyond 5 layers, a maximum intensity was observed at ≈300 nm, corresponding to the maximum absorption wavelength (Figure 4). Notably, a noteworthy linear correlation was identified between the LD intensity and the number of layers (i.e., thickness) (Figure 4 inset). Positive LD signals were recorded when the samples were aligned parallel to the incident cross-polarized light, while perpendicular orientation resulted in negative intensities, displaying perfect symmetry irrespective of the number of layers. It is worth noting that when the samples were set at 45° with respect to the light source either for a pure copolymer film or for a CNC-based film for which the orientation of CNC was not controlled, no LD signal was recorded.

In order to provide insights into the orientation of polymeric materials, polarized infrared spectroscopy can be useful because it gives selective information on the orientation state of polymeric chains.[42]

Horikawa et al. successfully utilized polarized FTIR for cellulose microfibrils, characterizing the uniplanar alignment of native cellulose microfibrils to the cell wall surface.[43] In this context, polarized FTIR analyses were conducted on samples comprising 10, 25, and 50 layers, both on the copolymer and on a sample where CNCs are not aligned in a preferential direction. Three orientations of the sample vis-a-vis the IR irradiation were considered including 0°, 45°, and 90°, (**Figure 5**a). Regardless of their orientation concerning the polarizer, the spectra containing cellulosic material exhibited the characteristic bands of nanocellulose.[44]

Upon examining the obtained spectra, it becomes evident that the pure copolymer sample and the non-oriented CNC sample exhibit no variation with the angle of analysis. On the other hand, and notably, the spectra of the materials made of 10, 25, and 50 layers are remarkably similar, demonstrating a consistent trend in variation with changing sample angles. Herein, only the spectra of the sample with 50 layers are presented, and similar observations can be made for materials with fewer layers. Zooms of the spectrum of the material loaded with 50 layers in the range of 3800–3000 and 1200–1000 cm^{-1} are displayed in Figure 5b,c, respectively. The peaks observed at 1065 and 1169 cm^{-1} correspond to the vibration of the C—O—C pyranose ring and antisymmetric stretching of the C—O bridge, respectively. Noticeably, stronger peaks are observed for the nanocomposite analyzed at 0° angle compared to the one at 90°. This suggests that the CNCs are oriented parallel to the polarization axis of the IR irradiation, corresponding to the withdrawal direction. At this 0° angle, the IR rays pass through the highest number of functional groups of the film. It is worth noting that the sample analyzed at an angle of 45° exhibits an intermediate behavior. As previously mentioned, FTIR analyses reveal consistent trends for samples with 10, 25, or 50 layers, indicating that the orientation is intrinsic to a single layer. Likewise, concerning the peak observed at 3350 cm^{-1}, which signifies the O—H stretching vibration, the intensity is higher when the sample is oriented at 0° with respect to the polarization axis compared to other orientations. The higher intensity of the O—H stretching peak at 3350 cm^{-1} for the non-oriented CNC sample may be due to the inherent random orientation of the CNCs, which allows for more uniform interaction with the polarized IR light across all angles.

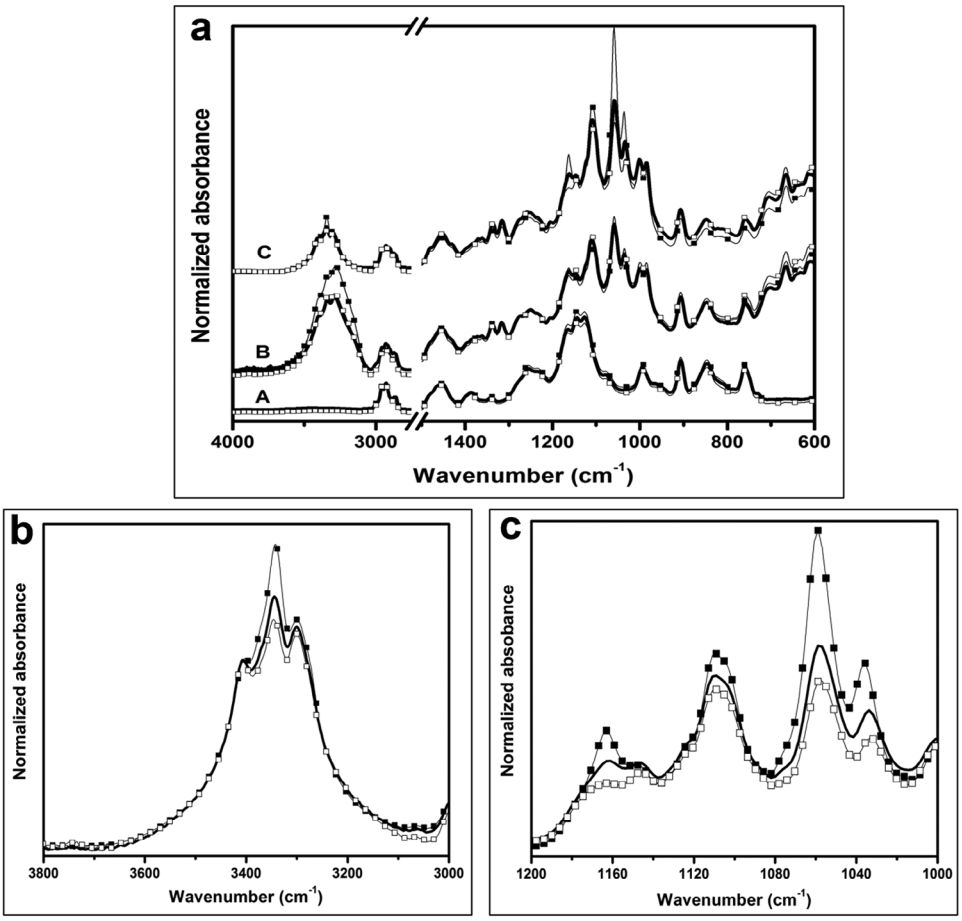

Figure 5. a) FTIR spectra depicting the poly(EHA-co-GMA) (A), a sample without aligned CNCs (B), and a sample comprising 50 layers of oriented CNCs (C) analyzed at angles of (■) 0°, (line) 45° and (□) 90° relative to the IR beam; b,c) close-ups of the FTIR spectra for the "50 layers" sample.

To further assess the versatility of this uncomplicated and cost-effective assembly approach for crafting optically active CNCs/poly(EHA-co-GMA), the materials were examined under polarized light. Illustrated in **Figure 6** are examples of the captured images. The films were positioned in the microscope at 0 and 45° relative to the deposition direction to alter the incident angle of light. Under parallel alignment of the polarizer and analyzer, and with the sample oriented in the deposition direction, an amber color devoid of distinctive features was observed (Figure 6). This color subtly transitioned to orange with an increasing number of deposited layers (not shown). When the nanocomposite was observed at 45° with respect to the withdrawal direction (Figure 6a,c), it exhibited strong selective reflections with uniform and intense colors dependent on the counts of stratified layers (blue-dominant for 25-layers and green-dominant for 50-layers). Thus, these selective colors confirm that the birefringence arises from light interferences within multilayered structures of thin films created by organized particles.[45] One assumes that CNC, with an ordinary refractive index of 1.58 and an extraordinary one of 1.53, embedded in a polymer matrix with a refractive index of 1.5 means that the birefringence would be ≈0.05, hence our results fall perfectly into the Michel Levy chart plotted based on such system. Hence, the iridescence observed in CNC-based films arises from the angle-dependent selective reflection of polarized light. The dominant color is fundamentally contingent on the degree of stratification (e.g., thickness) and its organization as observed in some living organisms, such as the fruit of *Pollia condensata*.[46] The observed homogenous and intense colors do not show any radial variation and heterogeneities commonly present in solvent-cast films and result from varying speeds of solvent evaporation during the passage of the drying front over the film, with faster evaporation occurring at the edges compared to the central part.[47–50] Intriguingly, in our case the uniformity of colors points out the absence of a mosaic of helical stacks compared to the CNCs oriented by magnetic field.[49] Indeed, helical stacks are usually formed from the spontaneous assembly of CNCs and not under force-driven alignment. Therefore, it can be concluded from Figures 4 and 6 that the observed colors of CNC oriented by the shear-driven convective method are not due to the chiral nematic structure but the birefringence. A parallel occurrence was noted in prior studies by Zhao et al., where the chiral long-range alignment of cholesteric CNCs was disrupted or dismantled through axial-centrifugal stretching during the spin-coating process.[32]

Besides, the highly organized structure obtained herein as well as the formation of a high-loading CNC percolated network should give rise to a unique material with reinforced mechanical properties as already reported for some bioinspired

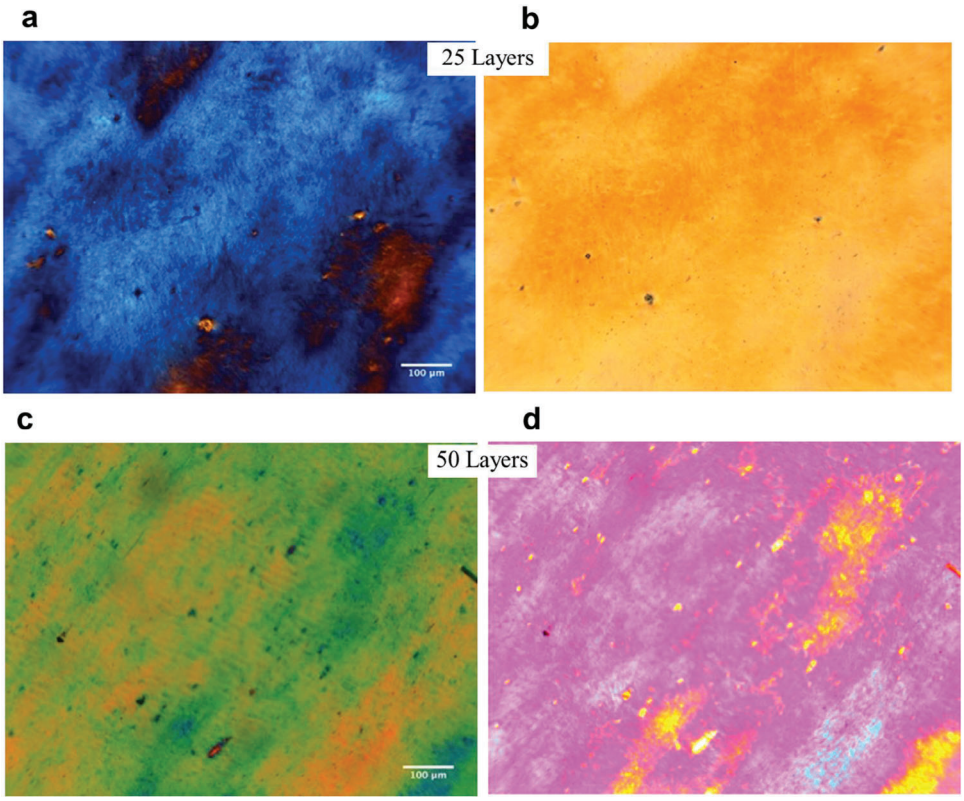

Figure 6. Optical micrographs of CNCs/poly(EHA-co-GMA) films deposited by shear-convective-assembly on glass substrate taken under polarized light with sample oriented 45° with respect to: (a and c) the direction of the deposition with the analyzer and polarizer parallel (b and d) the direction of the deposition with the analyzer and polarizer perpendicular (cross polarizer).

materials.[51,52] Indeed the modulus of the resulting films was estimated in our previous work by Peak-Force AFM to be ≈11–12 GPa.

Figure 7a shows that the maximum absorption wavelengths obtained by UV–vis absorption correlate with the positions of the LD signals maxima (≈310 nm). CD spectroscopy provides insights into the chiroptical properties of the films by assessing the differential absorption between left- and right-handed circularly polarized light, and has been widely applied to study CNCs.[53–55] To measure the CD spectra of the films, we used an integrating sphere installed in the sample chamber of the CD spectrophotometer. Figure 7b shows broad CD signals with a negative peak ≈310 nm for the film composed of 25 layers, whereas a positive CD signal is observed at the same wavelength for the film made of 50 layers. The inverse CD signals for the films with 25 layers and those with 50 layers are surprising and could be attributed to differences in the helicoidal stacking within the films, whereas for both films the broadness of the peaks and signal above 350 nm could be attributed to light scattering, as probed by CD signal detection with the integrated sphere.

3. Conclusion

In this study, a shear-convective assembly technique was employed to stratify multilayers of CNCs embedded in an acrylic-based polymer matrix. This process resulted in highly transparent and compact nanocomposite films, with a measured total thickness of ≈20 µm. AFM analysis revealed that CNCs in the uppermost layer were consistently aligned toward the withdrawal direction, with over 87% of CNCs oriented within ±20° of this direction. Importantly, the deposition of additional layers did not disturb the alignment of the sublayers, as confirmed by GISAXS and LD experiments. The films exhibited strong selective reflections, with the color intensity and hue varying based on the number of stratified layers blue-dominant for 25 layers and green-dominant for 50 layers. These optical properties suggest that the birefringence, estimated to be ≈0.05, arises from light interference within the multilayered structure. This matches well with the Michel-Levy chart, further confirming the organized structure of the films. This stratification approach presents a simple, fast, and cost-effective method for creating birefringent materials, offering potential applications in coatings, sensors, and optical devices.

4. Experimental Section

Materials: Before utilization, EHA (VWR, 99%) and tetrahydrofuran (THF, VWR, 99%) were subjected to passage through a basic alumina column to eliminate the stabilizing agent. GMA (VWR, 97%) underwent drying over anhydrous calcium hydride for 24 h at room temperature and purification through vacuum distillation at 60 °C before utilization. Azobisisobutyronitrile (AIBN, 98%), dimethylformamide (DMF, Acros, for analysis), sodium hydroxide (NaOH, Acros), sulfuric acid (Merck, 98%), and hydrogen peroxide (Sigma Aldrich, 30%) were employed in

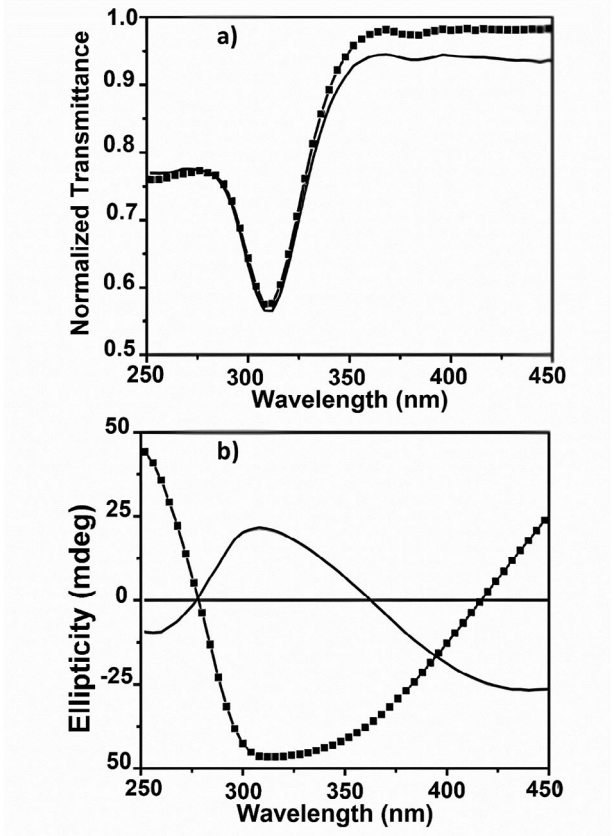

Figure 7. UV–vis transmission (a) and CD spectra (b) of CNCs/poly(EHA-co-GMA) films consisting of 25 layers (■) and 50 layers (line) using a CD integrating sphere.

their as-received states. Pure ramie fibers were sourced from Stucken Melchers GmbH & Co (Germany). Glass was used as a substrate for coating.

Free-Radical Copolymerization: The synthesis of the copolymer was achieved via free radical copolymerization in a THF.[36] The monomers (EHA:GMA in a 40:60 molar ratio) were dissolved in dried THF at a concentration of 2 M. The solution underwent meticulous degassing through several freeze–pump–thaw cycles. AIBN was then added to the flask to initiate polymerization. The flask was promptly placed in a thermostatic oil bath at 70 °C for 24 h with continuous stirring. Termination of the reaction was achieved by immersing the flask in liquid nitrogen, and the copolymer was precipitated from the solution using a THF:methanol mixture (1:7). Subsequently, it was filtered and dried at room temperature under vacuum (0.1 mbar) for 2 days (**Figure 8**A). Characterization of the obtained copolymer was performed using ^{1}H NMR spectroscopy (from previous work), confirming a molecular composition of 20% GMA and 80% EHA.[36]

Preparation of Cellulose Nanocrystals: 60 grams of meticulously purified ramie fibers were cut into small fragments and subjected to treatment with a 4% NaOH solution (1000 mL) at 80 °C for 2 h to eliminate residual contaminants. Following this, acid hydrolysis was carried out using an 800 mL solution of sulfuric acid (65% wt.) at 55 °C for 30 min, with continuous mechanical stirring. The resulting suspension underwent filtration through a sintered glass no.1 to remove macroscopic fragments from unhydrolyzed fibers. Through a thorough process of washing with water, achieved via centrifugation and dialysis against deionized water until neutralization, the suspension was concentrated to 4% to serve as the stock suspension. According to AFM analyses, the resultant CNCs exhibited an average length of ≈200 nm and an average width ranging from 7 to 10 nm.

Dispersion of Cellulose Nanocrystals in DMF: The transformation of an aqueous CNC suspension to DMF involved a solvent-exchange process. A specific volume of DMF was introduced into the aqueous CNC dispersion, and the resulting mixture was transferred to a 100 mL flask. Water was then removed by employing a rotavapor. Subsequently, the suspension underwent ultrasonication for 5 min to ensure the optimal dispersion of CNC. The concentration of the final suspension was determined gravimetrically and found to be 3.7% (wt.).

Processing of Nanocomposite Coatings: Before the film processing stage, a mixture of CNC and copolymer in DMF was formulated by dissolving 0.5 g of the copolymer in DMF. After solvent-exchange from water to DMF, the resultant CNC suspension was combined with the prepared poly(EHA-co-GMA) to obtain a suspension of CNCs/poly(EHA-co-GMA) with a weight ratio of 50/50.[30] The nanocomposite films were deposited using the shear-convective assembly method with DMF as the solvent and glass as the substrate. In preparation for deposition, the glass substrates underwent a meticulous cleaning process with a piranha solution for 30 min, followed by a thorough rinse with distilled water. The upper inclined plate, connected to a syringe pump motor assembly (Model Fusion 10) provided by KR Analytical Ltd, was maneuvered at a regulated speed of 4.8 m h^{-1}. The angle between the two plates remained fixed at 11.25° throughout all deposition processes. This setup was positioned in a laminar fume hood with positive airflow to prevent contamination. Subsequently, a volume of 10 µL of the resulting nanocomposite solution was deposited between the inclined plate and the glass substrate. After plate withdrawal, a dried ultra-thin film was formed. This procedure was repeated several times to achieve coatings with 10, 25, and 50 layers. Before depositing each successive layer, the film was left to dry for a few minutes to remove residual traces of DMF (Figure 8B).

Atomic Force, Optical and Scanning Electron Microscopies: Atomic force microscopy was performed to characterize the microscopic morphology properties of the coatings. The films were deposited on the silicon wafer and imaged using Peak Force Tapping (PFT) technique based on real-time force–distance curve analysis recorded at a cantilever frequency of ≈2 kHz using a Bruker ICON AFM. This technique provides high-resolution imaging and allows us to control the force applied between the sample and the tip to limit deformation or damage to the probe or sample. AFM images were performed in air and in ambient conditions with SNL-10 tips type with a spring constant of 0.35 Nm^{-1} and a radius of curvature of ≈10 nm.

CNC orientation of the top layer was scrutinized by the analysis of AFM images with the software Gwyddion. AFM images were examined, and individual CNCs were assigned to director vectors. The Gwyddion software was employed to calculate the relative angle of each vector to the withdrawal direction. Consequently, CNCs were sorted into distinct groups based on angles (0–20°, 20–40°, 40–60°, and 60–90°). Symmetry conditions were applied for angles ranging from -90° to 0°, with counts being aggregated to their corresponding positive angles Significantly, several hundreds of CNCs were tallied in each image analysis.

An Ultra High-Resolution Cold Field Emission Scanning Electron Microscope (FE-SEM) from Hitachi (model SU8020), operating between 100 V and 30 kV and equipped with 5 electron detectors in addition to a built-in EDS SDD detector from Thermo Scientific, was used to assess the coatings morphologies.

Linear Dichroism Spectroscopy: LD spectra were measured using a Chirascan Plus CD Spectrometer from Applied Photophysics, UK. A detector whose detection range is from 160 to 1150 nm permits to switch from CD standard analysis to a CS/LD linear dichroism detector. LD of an oriented molecule is the difference in the absorption of parallel and perpendicular linearly polarized light. Samples were set parallel, perpendicular, or at 45° with respect to the incident cross-polarized light and scanned at 120 nm min^{-1} with a step resolution of 0.2 and 1 nm bandwidth. The detector baseline corrections were made by subtracting the spectrum from the glass substrate blank.

UV–vis Transmission and Circular Dichroism Spectroscopy: UV–vis transmission and CD spectra were measured using the Chirascan Integrating Sphere accessory installed in the Chirascan sample chamber from

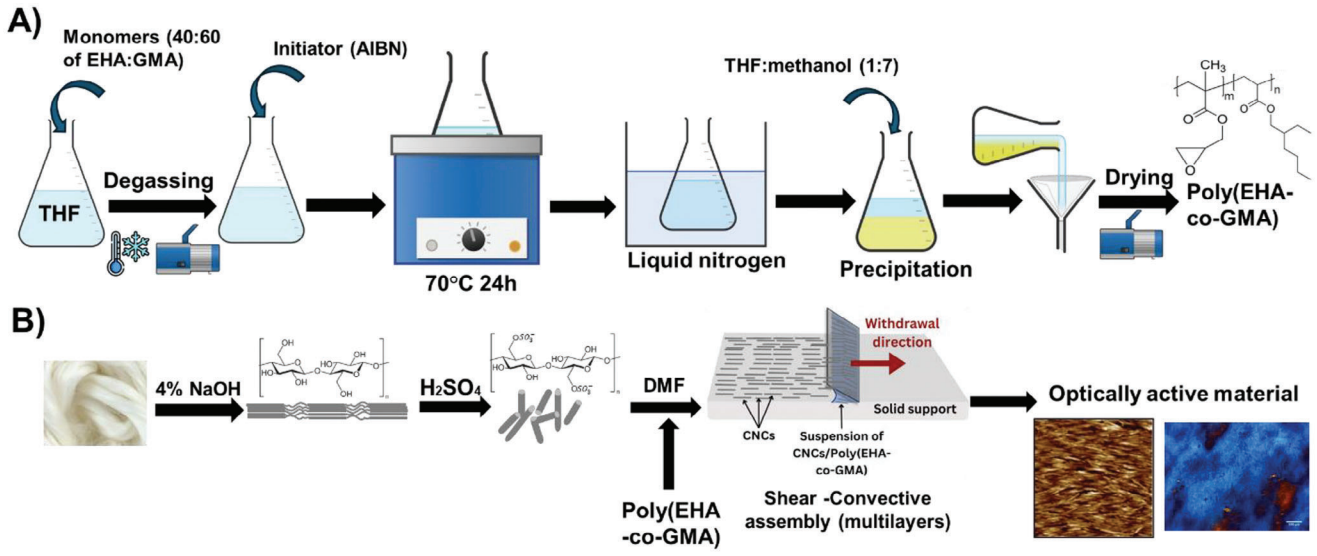

Figure 8. A schematic illustrating A) the synthesis protocol of the poly(EHA-co-GMA) and B) the isolation of CNCs from ramie fibers and their aligned assembly via the shear-convective method.

the Chirascan Plus CD Spectrometer from Applied Photophysics, UK. The CNCs/poly(EHA-co-GMA) films consisting of "25 layers" and "50 layers" were placed into the Chirascan Integrating Sphere in a diffuse reflectance mode, and the spectra were recorded between 250 and 450 nm, with a bandwidth of 1 nm, 120 nm min^{-1} with a step resolution of 0.2. The sample was rotated into the holder to minimize sample anisotropy artifacts. Blank spectra recorded for the glass substrate were used as baselines and were automatically subtracted from the UV and CD spectra of the samples. The spectrometer measures the differences in absorption of left- and right-handed CPL and this difference is expressed in terms of ellipticity in millidegrees (mdeg).

Synchrotron Grazing Incidence Small Angle X-Ray Scattering: The GISAXS experiments were performed at the high-flux Austrian SAXS beamline at Elettra synchrotron in Triest, Italy, which is well suited for studying time-resolved structural transitions with an X-ray energy of 8 keV (λ = 1.54 nm). The samples were mounted on a sample stage that can be rotated around two axes (e.g., transversal to the beam in 5 µm steps and tilted to set the incidence angle in millidegree steps). The sample-to-detector distance was determined to be 1.517 m via silver behenate calibration (lamellar spacing of 5.838 nm) and a 2D Pilatus 1 M Detector System was used with a 10-module array of each module having a size of 487 × 195 pixels (pixel size = 172 × 172 μm^2). Between the sample and detector, a vacuum tube was mounted to reduce the air scattering. The detector images were transferred into reciprocal space using the X-ray tool-library X-ray utilities. To obtain the 1D cuts, the Dectris freeware ALBULA 3.2.0 was used. The out-of-plane cut (q_y) as a function of constant q_z was extracted immediately above the Yoneda peak for each sample. The specular beam was set to ≈0.79° (above the critical angle of total reflection of organic thin films). Instead of using a structure factor, the peak positions and structural features were directly determined from the corresponding q_y values (kinematic SAXS regime).

Fourier Transform InfraRed Spectroscopy: Fourier Transform InfraRed (FTIR) spectroscopy measurements were carried out using a Bio-RAD Excalibur FTS 3000 FTIR spectrometer. The spectral range was 600 to 4000 cm^{-1}, with a resolution of 4 cm^{-1} and an accumulation of 32 scans. All spectra were normalized to the band at 1730 cm^{-1}, which corresponds to the carbonyl stretching frequency and remains unaffected by the addition of CNCs. Polarized spectra were obtained by placing a polarizer (Brukker, USA) in the path of the IR beam before it reached the sample. Measurements were taken with the samples oriented at 0°, 45°, and 90° relative to the beam.

Supporting Information

Supporting Information is available from the Wiley Online Library or from the author.

Acknowledgements

The authors are grateful to OCP group for the financial support under the SUSMAT Chair, Accord Specific number N 165 and to the "Région Wallonne" and European Community (FEDER, FSE) in the frame of "Pôle d'Excellence Materia Nova" and in the Valicell project for financial support. This work was also partially supported by the Fonds de la Recherche Scientifique – FNRS under the grants no. 1.B333.15F (CHIRNATES). M.S. is FNRS research director. Elettra Synchrotron is acknowledged for providing synchrotron radiation at the Austrian SAXS beamline.

Conflict of Interest

The authors declare no conflict of interest.

Data Availability Statement

Data sharing is not applicable to this article as no new data were created or analyzed in this study.

Keywords

acrylics, cellulose nanocrystals, controlled optical activity, hierarchical structure, ordered nanocellulose

Received: July 18, 2024
Revised: October 16, 2024
Published online:

[1] U. G. K. Wegst, H. Bai, E. Saiz, A. P. Tomsia, R. O. Ritchie, *Nat. Mater.* **2015**, *14*, 23.

[2] D. Stuart-Fox, L. Ospina-Rozo, L. Ng, A. M. Franklin, *Trends in Ecology & Evolution* **2021**, *36*, 187.
[3] Z. Xuan, J. Li, Q. Liu, F. Yi, S. Wang, W. Lu, *The Innovation* **2021**, *2*, 100081.
[4] F. Chen, Y. Huang, R. Li, S. Zhang, B. Wang, W. Zhang, X. Wu, Q. Jiang, F. Wang, R. Zhang, *Chem. Commun.* **2021**, *57*, 13448.
[5] B. Frka-Petesic, T. G. Parton, C. Honorato-Rios, A. Narkevicius, K. Ballu, Q. Shen, Z. Lu, Y. Ogawa, J. S. Haataja, B. E. Droguet, R. M. Parker, S. Vignolini, *Chem. Rev.* **2023**, *123*, 12595.
[6] Y. Habibi, L. A. Lucia, O. J. Rojas, *Chem. Rev.* **2010**, *110*, 3479.
[7] S. Fraden, G. Maret, D. L. D. Caspar, R. B. Meyer, *Phys. Rev. Lett.* **1989**, *63*, 2068.
[8] T. Folda, H. Hoffmann, H. Chanzy, P. Smith, *Nature* **1988**, *333*, 55.
[9] P. A. Buining, H. N. W. Lekkerkerker, *J. Phys. Chem.* **1993**, *97*, 11510.
[10] D. A. Marvin, *Curr. Opin. Struct. Biol.* **1998**, *8*, 150.
[11] F. Livolant, A. Leforestier, *Prog. Polym. Sci.* **1996**, *21*, 1115.
[12] Y. Yang, X. Wang, H. Huang, S. Cui, Y. Chen, X. Wang, K. Zhang, *Adv. Opt. Mater.* **2020**, *8*, 2000547.
[13] C. Hu, L. Bai, F. Song, Y. Wang, Y. Wang, *Carbohydr. Polym.* **2022**, *296*, 119929.
[14] N. Yang, X. Ji, J. Sun, Y. Zhang, Q. Xu, Y. Fu, H. Li, M. Qin, Z. Yuan, *Nanoscale* **2019**, *11*, 10088.
[15] G. Zhao, Y. Huang, C. Mei, S. Zhai, Y. Xuan, Z. Liu, M. Pan, O. J. Rojas, *Small* **2021**, *17*, 2103936.
[16] Y. Geng, P. Brogueira, J. L. Figueirinhas, M. H. Godinho, P. L. Almeida, *Liq. Cryst.* **2013**, *40*, 769.
[17] M. Giese, L. K. Blusch, M. K. Khan, W. Y. Hamad, M. J. MacLachlan, *Angew. Chem., Int. Ed.* **2014**, *53*, 8880.
[18] K. E. Shopsowitz, J. A. Kelly, W. Y. Hamad, M. J. MacLachlan, *Adv. Funct. Mater.* **2014**, *24*, 327.
[19] K. E. Shopsowitz, W. Y. Hamad, M. J. MacLachlan, *Angew. Chem., Int. Ed.* **2011**, *50*, 10991.
[20] C. Browne, V. S. Raghuwanshi, G. Garnier, W. Batchelor, *J. Colloid Interface Sci.* **2023**, *650*, 1064.
[21] C. Li, J. Evans, N. Wang, T. Guo, S. He, *Sci. Rep.* **2019**, *9*, 11290.
[22] A. Tran, W. Y. Hamad, M. J. MacLachlan, *ACS Appl. Nano Mater.* **2018**, *1*, 3098.
[23] W. Song, J.-K. Lee, M. S. Gong, K. Heo, W.-J. Chung, B. Y. Lee, *ACS Appl. Mater. Interfaces* **2018**, *10*, 10353.
[24] T.-D. Nguyen, W. Y. Hamad, M. J. MacLachlan, *Chem. Commun.* **2013**, *49*, 11296.
[25] Y.-D. He, Z.-L. Zhang, J. Xue, X.-H. Wang, F. Song, X.-L. Wang, L.-L. Zhu, Y.-Z. Wang, *ACS Appl. Mater. Interfaces* **2018**, *10*, 5805.
[26] R. Bardet, N. Belgacem, J. Bras, *ACS Appl. Mater. Interfaces* **2015**, *7*, 4010.
[27] C. C. Y. Cheung, M. Giese, J. A. Kelly, W. Y. Hamad, M. J. MacLachlan, *ACS Macro Lett.* **2013**, *2*, 1016.
[28] M. He, Y.-I. Hsu, H. Uyama, *Chem. Eng. J.* **2024**, *495*, 153516.
[29] I. Chae, D. Ngo, Z. Chen, A. L. Kwansa, X. Chen, A. B. Meddeb, N. J. Podraza, Y. G. Yingling, Z. Ounaies, S. H. Kim, *Adv. Mater. Interfaces* **2020**, *7*, 1902169.
[30] F. Khelifa, Y. Habibi, P. Leclère, P. Dubois, *Nanoscale* **2013**, *5*, 1082.
[31] F. Khelifa, M.-E. Druart, Y. Habibi, F. Bénard, P. Leclère, M. Olivier, P. Dubois, *Prog. Org. Coat.* **2013**, *76*, 900.
[32] Y. Zhao, G. Gao, D. Liu, D. Tian, Y. Zhu, Y. Chang, *Carbohydr. Polym.* **2017**, *174*, 39.
[33] H. M. A. Ehmann, S. Spirk, A. Doliška, T. Mohan, W. Gössler, V. Ribitsch, M. Sfiligoj-Smole, K. Stana-Kleinschek, *Langmuir* **2013**, *29*, 3740.
[34] K. M. O. Håkansson, A. B. Fall, F. Lundell, S. Yu, C. Krywka, S. V. Roth, G. Santoro, M. Kvick, L. Prahl Wittberg, L. Wågberg, L. D. Söderberg, *Nat. Commun.* **2014**, *5*, 4018.
[35] P. Klapetek, M. Valtr, D. Nečas, O. Salyk, P. Dzik, *Nanoscale Res Lett* **2011**, *6*, 514.
[36] F. Khelifa, Y. Habibi, F. Benard, P. Dubois, *J. Mater. Chem.* **2012**, *22*, 20520.
[37] D. Li, Z. Liu, M. Al-Haik, M. Tehrani, F. Murray, R. Tannenbaum, H. Garmestani, *Polym. Bull.* **2010**, *65*, 635.
[38] T. Pullawan, A. N. Wilkinson, S. J. Eichhorn, *Biomacromolecules* **2012**, *13*, 2528.
[39] S. Rocha, R. Kumar, B. Nordén, P. Wittung-Stafshede, *J. Am. Chem. Soc.* **2021**, *143*, 18899.
[40] P. Spaeth, S. Adhikari, M. D. Baaske, S. Pud, J. Ton, M. Orrit, *ACS Nano* **2021**, *15*, 16277.
[41] H. Takechi, K. Adachi, H. Monjushiro, H. Watarai, *Langmuir* **2008**, *24*, 4722.
[42] X. Luo, B. Lan, P. Wu, Q. Yang, *J. Appl. Polym. Sci.* **2023**, *140*, e53280.
[43] Y. Horikawa, T. Itoh, J. Sugiyama, *Cellulose* **2006**, *13*, 309.
[44] C. Trilokesh, K. B. Uppuluri, *Sci. Rep.* **2019**, *9*, 16709.
[45] R. K. Iler, *J. Colloid Interface Sci.* **1966**, *21*, 569.
[46] S. Vignolini, P. J. Rudall, A. V. Rowland, A. Reed, E. Moyroud, R. B. Faden, J. J. Baumberg, B. J. Glover, U. Steiner, *Proc. Natl. Acad. Sci., U. S. A.* **2012**, *109*, 15712.
[47] Z.-L. Zhang, X. Dong, Y.-N. Fan, L.-M. Yang, L. He, F. Song, X.-L. Wang, Y.-Z. Wang, *ACS Appl. Mater. Interfaces* **2020**, *12*, 46710.
[48] T. Chen, Q. Zhao, X. Meng, Y. Li, H. Peng, A. K. Whittaker, S. Zhu, *ACS Nano* **2020**, *14*, 9440.
[49] B. Frka-Petesic, G. Guidetti, G. Kamita, S. Vignolini, *Adv. Mater.* **2017**, *29*, 1701469.
[50] K. Uetani, H. Yano, *Soft Matter* **2013**, *9*, 3396.
[51] J. C. Weaver, G. W. Milliron, A. Miserez, K. Evans-Lutterodt, S. Herrera, I. Gallana, W. J. Mershon, B. Swanson, P. Zavattieri, E. DiMasi, D. Kisailus, *Science* **2012**, *336*, 1275.
[52] S. Nikolov, M. Petrov, L. Lymperakis, M. Friák, C. Sachs, H.-O. Fabritius, D. Raabe, J. Neugebauer, *Adv. Mater.* **2010**, *22*, 519.
[53] R. Xiong, S. Yu, S. Kang, K. M. Adstedt, D. Nepal, T. J. Bunning, V. V. Tsukruk, *Adv. Mater.* **2020**, *32*, 1905600.
[54] J. Majoinen, J. Hassinen, J. S. Haataja, H. T. Rekola, E. Kontturi, M. A. Kostiainen, R. H. A. Ras, P. Törmä, O. Ikkala, *Adv. Mater.* **2016**, *28*, 5262.
[55] R. Mujica, A. Augustine, M. Pauly, Y. Battie, G. Decher, V. L. Houérou, O. Felix, *Adv. Mater.* **2024**, *36*, 2401742.